Multipartite Mixed-Species Entanglement over a Quantum Network

D. Main,* P. Drmota, E. M. Ainley, A. Agrawal, D. Webb, S. Saner, O. Băzăvan, B. C. Nichol, R. Srinivas, D. P. Nadlinger, G. Araneda,[†] and D. M. Lucas Department of Physics, University of Oxford, Clarendon Laboratory, Parks Road, Oxford OX1 3PU, United Kingdom

We generate multipartite entangled states of two, three and four matter qubits, where the entanglement is distributed over macroscopic distances via a photonic network link. Trapped-ion $^{88}\mathrm{Sr}^+$ qubits are entangled directly via the optical fibre link, and the entanglement is subsequently extended to $^{43}\mathrm{Ca}^+$ memory qubits co-trapped in each network node, using local mixed-species logic gates. We create remotely entangled Sr^+ - Ca^+ and Ca^+ - Ca^+ states, as well as mixed-species Greenberger-Horne-Zeilinger (GHZ) states of up to four qubits. We demonstrate storage of the remotely-entangled memory qubits for $\sim 10\,\mathrm{s}$, more than $100\times$ the creation time.

INTRODUCTION

Quantum networks enable the distribution of entanglement between physically separated systems. This capability is critical for a variety of quantum technologies such as entanglement-based cryptography [1], distributed quantum computing [2–4], quantum sensing [5], and metrology [6]. Many of these applications are based on the ability to repeatedly generate multipartite entangled states between separated modules during the execution of a protocol. Realising these applications requires network modules that can not only establish remote entanglement but also process and store quantum information locally between subsequent rounds of entanglement generation. Therefore, integrating robust quantum memories with photonic interfaces into quantum networking modules is essential [7–11].

The generation of multipartite entanglement across network nodes is a key milestone towards scalable architectures. Multipartite entangled states underpin many advanced quantum networking protocols, such as networked quantum error correction, quantum secret sharing, and distributed sensing with entanglement-enhanced sensitivity [12–14]. Demonstrating such states in real networks is therefore essential to benchmark performance beyond bipartite entanglement.

At the same time, supporting multiple types of qubits within a quantum network is critical to building heterogeneous modular systems that combine the strengths of different types of qubits, such as optimal photonic coupling, high-fidelity logic, or long-lived memory [15–19]. Crossqubit entanglement opens the door to hybrid quantum networks that can integrate diverse platforms or future-proof evolving hardware.

Trapped ions are among the leading candidates for quantum information processing due to their long coherence times [20], high-fidelity quantum gates [19, 21–27], and robust state preparation and measurement proto-

cols [28–30]. Furthermore, trapped ions naturally interface with optical photons, and photonic interconnects between ion-based modules have demonstrated state-of-theart networking capabilities, enabling the generation of remote entanglement between qubits separated by macroscopic distances [31–34].

In this Letter, we present an elementary quantum network consisting of two mixed-species trapped-ion modules—each containing one $^{88}\mathrm{Sr}^+$ ion and one $^{43}\mathrm{Ca}^+$ ion—where the $^{88}\mathrm{Sr}^+$ ion serves as the network interface and the $^{43}\mathrm{Ca}^+$ ion provides a robust quantum memory [35]. We demonstrate the integration of local mixed-species operations with quantum networking by generating bipartite entangled states and multipartite Greenberger-Horne-Zeilinger (GHZ) states of up to four qubits. We also show enhanced storage of remote entanglement using the $^{43}\mathrm{Ca}^+$ memory qubits, preserving entanglement between the modules for more than $10\,\mathrm{s}$, which greatly exceeds the entanglement generation timescale ($\sim 100\,\mathrm{ms}$).

QUANTUM NETWORKING MODULES

The quantum networking apparatus comprises two trapped-ion modules connected by a quantum optical link, as depicted in Fig. 1(a). Each module comprises an ultra-high vacuum chamber containing a microfabricated surface-electrode Paul trap, which is used to co-trap one ⁸⁸Sr⁺ and one ⁴³Ca⁺ ion (see Supplementary Information S1). A $\sim 0.5 \,\mathrm{mT}$ magnetic field sets the quantisation axis and lifts the Zeeman state degeneracies, enabling the selection of pairs of energy states to form qubits, as outlined in Fig. 1(b) and (c). Specifically, ⁸⁸Sr⁺ provides an optical network qubit, $Q_{\rm N} = \{|0_{\rm N}\rangle \equiv |S_{1/2}, m_J = -\frac{1}{2}\rangle, |1_{\rm N}\rangle \equiv |D_{5/2}, m_J = -\frac{3}{2}\rangle\}$. The ground hyperfine manifold of $^{43}\mathrm{Ca^{+}}$ provides a long-lived *circuit* qubit, $\mathcal{Q}_{\mathrm{C}} = \{|0_{\mathrm{C}}\rangle \equiv$ $|F=4, m_F=0\rangle, |1_{\rm C}\rangle \equiv |F=3, m_F=0\rangle\},$ which has a first-order magnetic-field sensitivity of $122 \,\mathrm{kHz}\,\mathrm{mT}^{-1}$ at 0.5 mT, roughly two orders of magnitude lower than that of the network qubit. In addition, an auxiliary qubit is defined in the ground hyperfine manifold of ${}^{43}\text{Ca}^+$, $\mathcal{Q}_X =$

^{*} Current address: Oxford Ionics, Oxford, OX5 1GN; dougal.main@oxionics.com

 $^{^{\}dagger}$ gabriel.aranedamachuca@physics.ox.ac.uk

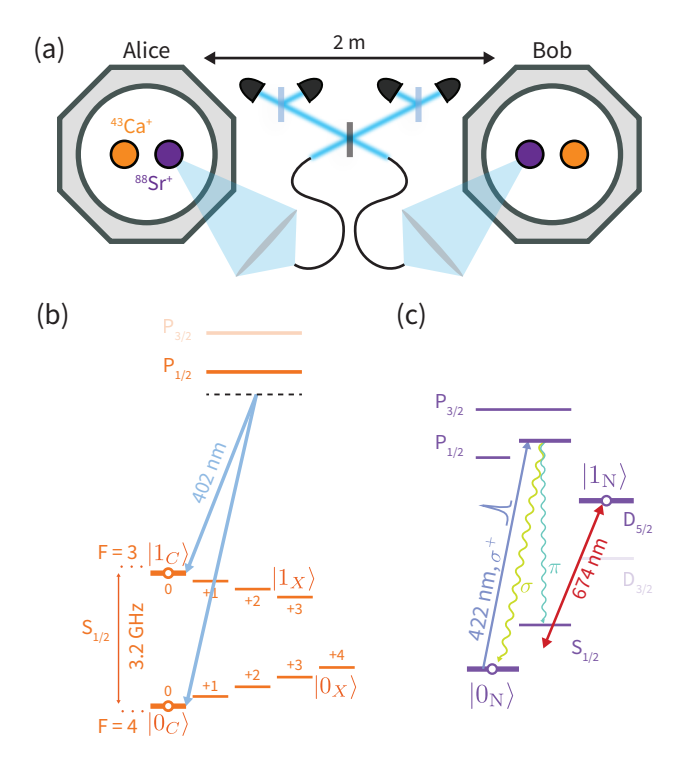


Fig. 1. Overview of mixed-species trapped-ion quantum networking apparatus. (a) Two modules, Alice and Bob, each co-trap one 88Sr⁺ and one ⁴³Ca⁺. High-numerical-aperture lenses collect single photons from the $^{88}\mathrm{Sr}^+$ ions and couple them into optical fibres. The photons are interfered at a central heralding station, where particular detection patterns herald the generation of entanglement between the Sr⁺ ions in each module. (b) The ground hyperfine manifold of ⁴³Ca⁺ provides a robust memory qubit, $\{|0_{\rm C}\rangle, |1_{\rm C}\rangle\}$, and an auxiliary qubit $\{|0_X\rangle, |1_X\rangle\}$. Transitions between the states within this manifold are driven using a pair of 402 nm Raman beams. (c) The ⁸⁸Sr⁺ ion provides a network qubit, $\{|0_N\rangle, |1_N\rangle\}$, which is connected by the optical 674 nm quadrupole transition. Ion-photon entanglement is generated via the rapid excitation of the Sr⁺ ion and subsequent decay via the 422 nm transition, generating entanglement between the polarisation state of the spontaneously emitted photon and the ground Zeeman states of the $^{88}\mathrm{Sr}^+$ ion.

 $\{|0_{\rm X}\rangle \equiv |F=4,m_F=+4\rangle, |1_{\rm X}\rangle \equiv |F=3,m_F=+3\rangle\}.$ The auxiliary qubit is used in the state preparation and measurement of the circuit qubit, as well as for mediating mixed-species quantum logic.

Within each module, laser beams are used for cooling, state preparation, coherent manipulation, and fluorescence detection of each species of ion. Single-qubit rotations of the $\mathcal{Q}_{\rm C}$ and $\mathcal{Q}_{\rm X}$ qubits are implemented using a pair of co-propagating 402 nm Raman beams; single-qubit rotations of the optical network qubit, $\mathcal{Q}_{\rm N}$, are implemented using a 674 nm laser to drive the quadrupole transition connecting the qubit states, as

shown in Fig. 1. To perform mixed-species entangling gates between the two ions, we follow Ref. [19] in which the interference pattern generated by a pair of non-copropagating Raman beams gives rise to a $\sigma_z \otimes \sigma_z$ -type spin-dependent force (see Supplementary Information). This spin-dependent force is used to implement geometric phase gates between the \mathcal{Q}_N and \mathcal{Q}_X qubits. As this gate mechanism does not couple to the \mathcal{Q}_C qubit, we require the ability to coherently inter-convert between the \mathcal{Q}_C and \mathcal{Q}_X qubits. This conversion is performed using the co-propagating Raman beams to coherently address the transitions within the ground hyperfine manifold of Ca⁺ (see Supplementary Information).

Complementing the ability to perform local quantum operations with the two ions in each module, another critical tool is the ability to establish remote entanglement between the two network qubits in separate modules. This is achieved using a two-photon try-until-success protocol, outlined in Ref. [32]. Each entanglement generation attempt begins with the preparation of the Sr⁺ ion in each module in the $|\downarrow\rangle = |S_{1/2}, m_J = -\frac{1}{2}\rangle$ state in the ground Zeeman manifold using approximately 320 ns of optical pumping. A ~10 ps pulse of σ^+ polarised 422 nm light excites the Sr⁺ ion to the $|P_{1/2}, m_J = +\frac{1}{2}\rangle$ state, which has a lifetime of 7 ns. The excited state decays to the ground Zeeman states, resulting in the spontaneous emission of a 422 nm photon [36]. The spontaneouslyemitted photons are collected from each module using high-numerical-aperture imaging systems, which couple the photons into single-mode optical fibres. These fibres bring the spontaneously-emitted photons from each module to a central heralding station, where a projective Bell state measurement is performed on the photons. Particular measurement outcomes herald the successful generation of entanglement between the Zeeman states of the Sr⁺ ions in the two modules. Finally, a 674 nm pulse maps one of the Zeeman states into the $D_{5/2}$ manifold, thereby establishing the remote entanglement of network qubits.

CHARACTERISATION OF ENTANGLED STATES

In this work, we combine the ability to generate remote entanglement between trapped-ion modules with local mixed-species quantum logic to create higher-dimensional entangled states. In particular, we consider N-particle states of the form

$$|\psi\rangle = \frac{|0\rangle^{\otimes N} + e^{i\varphi} |1\rangle^{\otimes N}}{\sqrt{2}},\tag{1}$$

where for N=2, this is the $|\Phi^{+}\rangle$ Bell-state, and for N>2, this is the N-particle GHZ state, up to a phase φ .

We characterise the generated multipartite states using both partial [37] and full state tomography (see Supplementary Information). Full state tomography enables

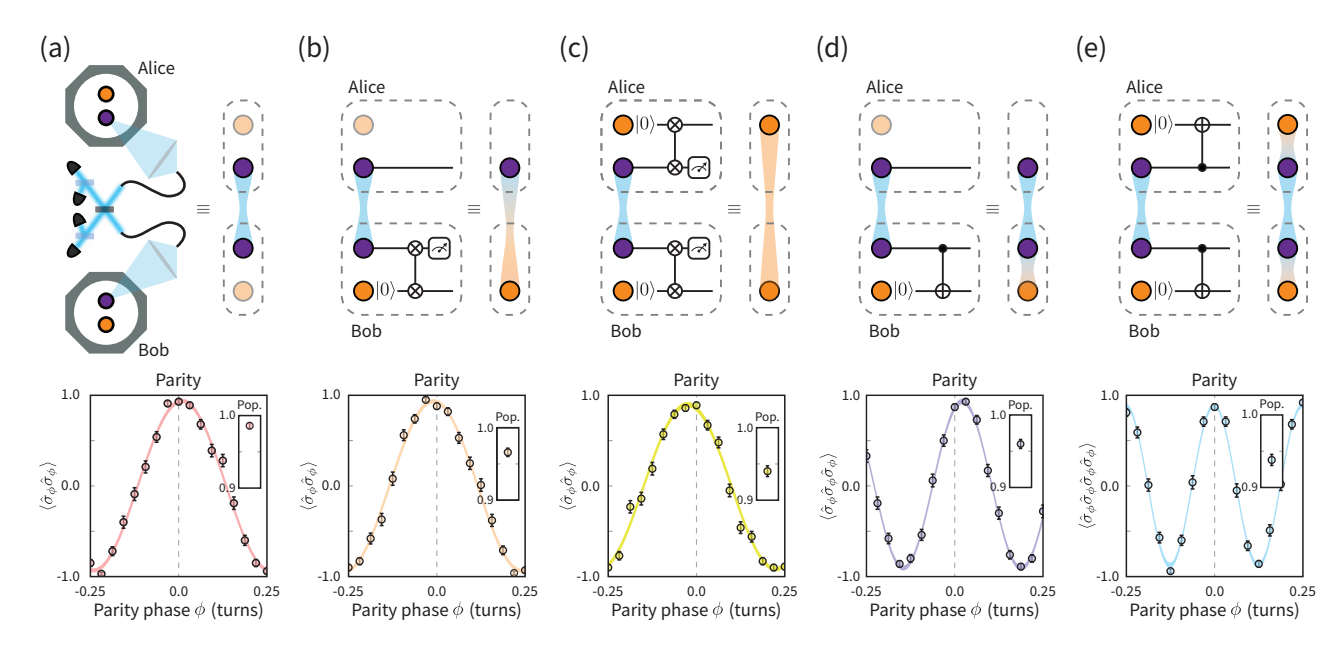


Fig. 2. Partial state tomography of the mixed-species remotely entangled states. (a) "Raw" Sr⁺-Sr⁺ entanglement. (b) Sr⁺-Ca⁺ entanglement, created using an error-detected iSWAP. (c) Ca⁺-Ca⁺ entanglement, created using error-detected iSWAPs. (d) 3-qubit GHZ state, created using a CNOT gate. (e) 4-qubit GHZ state, created using CNOT gates. Parity measurements are shown below each circuit, with insets displaying the population measurements. The shaded regions represents the 95 % confidence interval of the fit given by Eq. 2. The error bars on the measurements indicate one standard deviation. The inferred remote entanglement fidelities are given in Table I.

Io	Ions		Fidelity		iSWAP Error Prob.	Total Success Prob.	Average Rate
Alice	Bob		PST	FST		$\times 10^{-4}$	s^{-1}
Sr^+	Sr^+	$ 0_{N}0_{N}\rangle+ 1_{N}1_{N}\rangle$	96.0(7) %	96.94(9) %	_	1.236(3)	39.31(9)
Sr^+	Ca^{+}	$ 0_{\rm N}0_{\rm X}\rangle + 1_{\rm N}1_{\rm X}\rangle$	95.1(8)%	94.1(6)%	4.2(2)%	1.03(1)	7.14(7)
Ca^+	Ca^{+}	$ 0_X0_X\rangle + 1_X1_X\rangle$	92(1)%	93.1(7)%	8.4(3)%	1.24(1)	8.6(1)
Sr^+	$\mathrm{Sr}^+,\mathrm{Ca}^+$	$\begin{array}{l} 0_{\mathrm{N}}0_{\mathrm{N}}0_{\mathrm{X}}\rangle + \\ 1_{\mathrm{N}}1_{\mathrm{N}}1_{\mathrm{X}}\rangle \end{array}$	94(1)%	93.1(7)%	_	1.20(1)	8.26(8)
Sr^+, Ca^+	$\mathrm{Sr}^+,\mathrm{Ca}^+$	$\begin{array}{l} 0_{\mathrm{N}}0_{\mathrm{N}}0_{\mathrm{X}}0_{\mathrm{X}}\rangle + \\ 1_{\mathrm{N}}1_{\mathrm{N}}1_{\mathrm{X}}1_{\mathrm{X}}\rangle \end{array}$	91(1)%	91.9(8)%	-	1.44(2)	9.9(1)

Table I. Summary of mixed-species remotely entangled states characterised in this work. This table includes the observed entanglement fidelities extracted from both partial and full state tomography. The density matrices extracted from full state tomography can be found in the supplementary material (see Supplementary Information).

the complete reconstruction of the density matrix representing the quantum state of the ions from a tomographically complete set of single-qubit measurements. Partial state tomography assumes that the ideal target states have the form given by Eq. 1; thus to characterise the fidelity of the produced state to a particular target state, it is sufficient to perform population measurements, i.e., measurements of all qubits in the compu-

tational basis to determine $P = \mathbb{P}\left(|0\rangle^{\otimes N}\right) + \mathbb{P}\left(|1\rangle^{\otimes N}\right)$, and parity measurements, i.e., measurements of all qubits in the $\hat{\sigma}_{\phi} = \cos(\phi)\hat{\sigma}_{x} + \sin(\phi)\hat{\sigma}_{y}$ basis. Given quantum states of the form of Eq. 1, we anticipate that the expectation values for the parity measurements will be of the

form

$$\left\langle \bigotimes_{n=1}^{N} \hat{\sigma}_{\phi,n} \right\rangle = C \cos(N\phi - \varphi), \tag{2}$$

where C and φ are the parity contrast and phase, respectively. By performing these population/parity measurements, we can estimate the fidelity to the target state, up to the parity phase offset, as

$$\mathcal{F} = \frac{P+C}{2}.\tag{3}$$

A summary of all the entanglement fidelities and average generation rates for the remotely entangled states generated in this work is given in Table I.

Bipartite mixed-species entanglement

We first characterise remotely entangled bipartite states, i.e., states with N=2, starting with the remote entanglement of two network qubits, shown in Fig. 2(a). Full state tomography with 200 000 tomographic measurements of the Sr⁺-Sr⁺ ions yielded a density matrix representing a state with an entanglement fidelity of 96.94(9) %. This is consistent with the results of partial state tomography, shown in Fig. 2(a), which yielded a fidelity of 96.0(7) %. The average entanglement generation success probability was measured to be $1.236(3) \times 10^{-4}$. We suppress excess heating during entanglement generation by interleaving 500 us of entanglement generation attempts with approximately 320 µs of Doppler cooling and 500 µs of electromagnetically induced transparency (EIT) cooling. Including this cooling, we observe a net entanglement generation rate of $39.31(9) \,\mathrm{s}^{-1}$.

We combine this remote entanglement generation between each module's network qubits with local operations to create mixed-species entangled states. In particular, we use local mixed-species iSWAP gates to transfer the quantum states of the remotely entangled network qubits to the Ca⁺ auxiliary qubits, thereby enabling the generation of remotely entangled Sr⁺-Ca⁺ and Ca⁺-Ca⁺ states, as shown in Fig. 2(b) and (c), respectively. To enhance the fidelity of this quantum state transfer process, we perform mid-circuit measurements of the Sr⁺ ions after the iSWAP gates to detect errors in the mixed-species gates (see Supplementary Information). The modules exchange the outcomes of these measurements in real time via a classical communication link connecting the two control systems, allowing them to abort and restart the experiment if either module detects an error.

As with the Sr^+ - Sr^+ entangled state, we characterise the Sr^+ - Ca^+ and Ca^+ - Ca^+ remotely entangled states using both full and partial state tomography. Full state tomography with 10 000 tomographic measurements yielded density matrices representing states with entanglement fidelities of 94.1(6) % and 93.1(7) % for the

Sr⁺-Ca⁺ and Ca⁺-Ca⁺ states, respectively. The parity/population measurements for the Sr⁺-Ca⁺ and Ca⁺-Ca⁺ states are shown in Fig. 2(b) and Fig. 2(c), respectively. From these measurements, we extract entanglement fidelities of 95.1(8)% and 92(1)% for the Sr⁺-Ca⁺ and Ca⁺-Ca⁺ states, respectively. For these experiments, we interleave 200 µs of entanglement generation attempts with 500 µs of Doppler cooling and 500 µs of EIT cooling using the Sr⁺ ions since the local mixed-species operations require the ion crystal to be cooled to close to its motional ground state, resulting in an overall reduction of entanglement generation rate. This cooling sequence allows us to achieve average phonon numbers of the two-qubit gate motional mode of $\bar{n} \sim 0.15$ and $\bar{n} \sim 0.1$ in Alice and Bob, respectively.

Multipartite mixed-species entanglement

We go on to generate multipartite entangled states using the mixed-species trapped-ion modules. As shown in Fig. 2(d) and Fig. 2(e), these states are generated by first creating a $|\Phi^+\rangle$ Bell state between the network qubits in each module, followed by local mixed-species CNOT gates to entangle the Ca⁺ auxiliary qubits with the network qubits, creating the states in Eq. 1 with N=3 and N=4, respectively.

Full state tomography with 10 000 tomographic measurements yielded density matrices representing states with entanglement fidelities of 93.1(7)% and 91.9(8)% for the 3-qubit and 4-qubit GHZ states, respectively. The parity/population measurements for the 3-qubit and 4-qubit GHZ states are shown in Fig. 2(d) and Fig. 2(e), respectively. From these measurements, we extract entanglement fidelities of 94(1)% and 91(1)% for the 3-qubit and 4-qubit GHZ states, respectively.

STORAGE OF REMOTE ENTANGLEMENT

The ability to faithfully preserve quantum information in the modules on timescales longer than the time taken to generate remote entanglement is critical for many quantum networking applications. In the mixed-species experiments presented so far, the additional cooling required to implement the mixed-species operations means that this timescale is on the order of 100 ms. We have observed coherence times of the network qubit of approximately 8 ms; while this can be somewhat extended using dynamical decoupling, it is not sufficient for practical applications. We therefore utilise the long-lived circuit qubit in ⁴³Ca⁺ to gain access to a long-lived memory qubit. In previous work, we demonstrated the integration of this circuit qubit into one of our network modules [35]; we stored the ionic half of an ion-photon Bell pair for up to 10 s, and demonstrated that the storage was robust to network activity, i.e., the simultaneous generation of photons using the co-trapped Sr⁺ ion. Here, we extend this

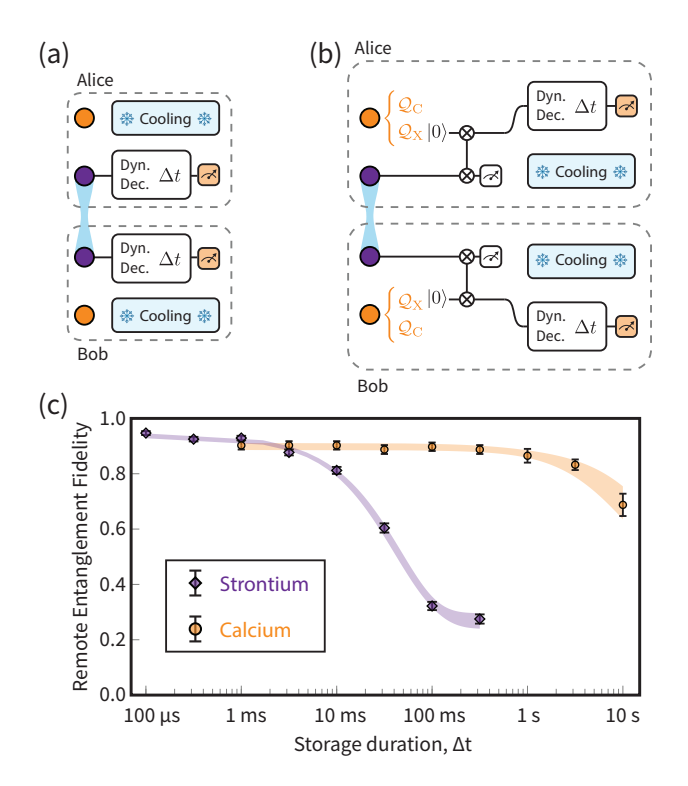


Fig. 3. Demonstration of the long-lived storage of remote entanglement. Circuits for probing the remote entanglement fidelity as a function of storage duration for (a) two network qubits and (b) two circuit qubits. Sympathetic cooling via the unused ion species and dynamical decoupling is performed to extend the storage capabilities of each qubit. (c) Remote entanglement fidelity as a function of storage duration for each qubit. Exponential decay fits (shaded bands) yield decay time constants of 44(3) ms and 14(4)s for the network and circuit qubits, respectively. All error bars indicate one standard deviation.

to both modules, thereby enabling the long-lived storage of entanglement between remote matter qubits.

In order to demonstrate the storage enhancement provided by our circuit qubits, we compare the abilities of the network and circuit qubits to store remote entanglement, measuring the fidelity as a function of storage duration. The experimental circuits used to characterise the storage capabilities of the qubits are shown in Fig. 3(a) and (b). The first step is to generate entanglement between the desired pair of gubits. For the network gubits, this is achieved as described above. To generate the remote entanglement between the circuit qubits, we first use error-detected iSWAP-gates to map the entanglement from the network to the auxiliary qubits (see Supplementary Information), before using a pair of Raman beams to coherently map the quantum information from the auxiliary qubits to the circuit qubits (see Supplementary Information).

With the entanglement created, we store the states for

a variable storage duration Δt . We deploy universally robust (UR) dynamical decoupling [38] to suppress sources of dephasing. The lengths of the UR sequence was adjusted for each storage duration, ranging from 4 pulses (UR4) to 48 pulses (UR48). Additionally, over this duration, the ion species not used to store the entanglement is used as a sympathetic coolant to prevent ion loss and mitigate single-qubit rotation errors due to heating. Finally, we perform parity and population measurements to estimate the fidelity of the entanglement after storage.

The fidelities of the stored entanglement as a function of storage duration for the two types of qubit is shown in Fig. 3(c). For the network qubit, we observe a significant degradation in the stored entanglement for storage durations exceeding 10 ms. We attribute this to the relatively high sensitivity of the network qubits to magnetic field fluctuations ($-11\,\mathrm{MHz\,mT^{-1}}$). Additionally, we observe that the fidelity of the network qubit entanglement decays below 50 % at storage durations exceeding 100 ms, indicating the presence of amplitude damping processes such as the decay of the $|1_\mathrm{N}\rangle$ state due to the finite lifetime of the $^{88}\mathrm{Sr^+}$ metastable $\mathrm{D}_{5/2}$ manifold (approximately 390 ms [39]). We fit an exponential decay to the fidelities, extracting a decay time constant of 44(3) ms for the network qubits.

For the circuit qubits, we observe a marked enhancement of the storage capability, observing a remote entanglement fidelity of 69(4)% after 10 s. Using the same exponential decay model as above, we extract a decay time constant of 14(4) s. This significantly exceeds the average time taken to generate entanglement in the mixed-species experiments ($\sim 100 \, \mathrm{ms}$).

DISCUSSION

In this Letter, we have demonstrated the integration of remote entanglement generation between trapped-ion modules with local mixed-species quantum logic. Specifically, we have realised bipartite entangled states between Sr⁺-Sr⁺, Sr⁺-Ca⁺, and Ca⁺-Ca⁺ ion pairs, as well as 3-qubit and 4-qubit multi-species GHZ states. All entangled states were generated with fidelities in the range of 91 % to 97 %.

We have also shown that remote entanglement can be reliably stored for more than $10\,\mathrm{s}$ in the long-lived circuit qubits of $^{43}\mathrm{Ca}^+$, a duration approximately two orders of magnitude longer than the average entanglement generation time. This capability is critical for protocols requiring multiple instances of entanglement generation, such as entanglement distillation [40], where storage buffers are essential.

The demonstrated ability to generate, manipulate, and store remotely entangled states across different ion species represents a key enabling technology for future quantum networks. These techniques are complementary to those being developed to operate a quantum network within the omg architecture [41–43]. Heterogeneous

entanglement—such as that between different atomic species—can be utilised for advanced applications, including enhanced frequency comparisons in atomic clock networks. In such networks, entangled states engineered across species with complementary sensitivities can yield improved stability and reduced systematic uncertainties [44], or enable remote quantum logic spectroscopy [15].

Moreover, the generation of multipartite entangled states across remote modules opens pathways to enhanced remote sensing protocols [6, 45, 46], and could serve as a distributed entanglement resource for quantum error correction in networked quantum computing architectures [12, 47].

- Ekert, A. K. Quantum cryptography based on bell's theorem. Phys. Rev. Lett. 67, 661 (1991).
- [2] Cirac, J. I., Ekert, A. K., Huelga, S. F. & Macchiavello, C. Distributed quantum computation over noisy channels. Phys. Rev. A 59, 4249 (1999).
- [3] Jiang, L., Taylor, J. M., Sørensen, A. S. & Lukin, M. D. Distributed quantum computation based on small quantum registers. Phys. Rev. A 76, 062323 (2007).
- [4] Main, D. et al. Distributed quantum computing across an optical network link. Nature 638, 383 (2025).
- [5] Guo, X. et al. Distributed quantum sensing in a continuous-variable entangled network. Nature Physics 16, 281 (2020).
- [6] Kómár, P. et al. A quantum network of clocks. Nat. Phys. 10, 582 (2014).
- [7] Kimble, H. J. The quantum internet. Nature 453, 1023 (2008).
- [8] Reiserer, A. & Rempe, G. Cavity-based quantum networks with single atoms and optical photons. Reviews of Modern Physics 87, 1379 (2015).
- [9] Wehner, S., Elkouss, D. & Hanson, R. Quantum internet: A vision for the road ahead. Science 362 (2018).
- [10] Pompili, M. et al. Realization of a multinode quantum network of remote solid-state qubits. Science **372**, 259 (2021).
- [11] Hucul, D. et al. Modular entanglement of atomic qubits using photons and phonons. Nature Physics 11, 37 (2015).
- [12] Gottesman, D. & Chuang, I. L. Demonstrating the viability of universal quantum computation using teleportation and single-qubit operations. Nature 402, 390 (1999).
- [13] Hillery, M., Bužek, V. & Berthiaume, A. Quantum secret sharing. Physical Review A 59, 1829 (1999).
- [14] Komar, P. et al. A quantum network of clocks. Nature Physics 10, 582 (2014).

ACKNOWLEDGEMENTS

We thank Chris Ballance, Joe Goodwin, Laurent Stephenson, Péter Juhász, and Jake Blackmore for their contributions to the design and construction of the apparatus, Sandia National Laboratories for supplying the ion traps used in this experiment, and the developers of the control system ARTIQ [48]. DM acknowledges support from the U.S. Army Research Office (ref. W911NF-18-1-0340). DPN acknowledges support from Merton College, Oxford. EMA acknowledges support from the U.K. EPSRC "Quantum Communications" Hub EP/T001011/1. RS acknowledges funding from an EP-SRC Fellowship EP/W028026/1 and Balliol College, Oxford. GA acknowledges support from Wolfson College, Oxford and Cisco. This work was supported by the U.K. EPSRC "Quantum Computing and Simulation" Hub EP/T001062/1. RS is partially employed by Oxford Ionics Ltd. DML consults for Quantinuum. The remaining authors declare no competing interests.

- [15] Schmidt, P. O. et al. Spectroscopy using quantum logic. Science 309, 749 (2005).
- [16] Tan, T. R. et al. Multi-element logic gates for trappedion qubits. Nature 528, 380 (2015).
- [17] Inlek, I. V., Crocker, C., Lichtman, M., Sosnova, K. & Monroe, C. Multispecies trapped-ion node for quantum networking. Physical review letters 118, 250502 (2017).
- [18] Bruzewicz, C., McConnell, R., Stuart, J., Sage, J. & Chiaverini, J. Dual-species, multi-qubit logic primitives for ca+/sr+ trapped-ion crystals. npj Quantum Information 5, 102 (2019).
- [19] Hughes, A. C. et al. Benchmarking a high-fidelity mixed-species entangling gate. Phys. Rev. Lett. 125, 080504 (2020).
- [20] Wang, P. et al. Single ion qubit with estimated coherence time exceeding one hour. Nat. Commun. 12, 233 (2021).
- [21] Ballance, C. J., Harty, T. P., Linke, N. M., Sepiol, M. A. & Lucas, D. M. High-fidelity quantum logic gates using trapped-ion hyperfine qubits. Phys. Rev. Lett. 117, 060504 (2016).
- [22] Gaebler, J. P. et al. High-fidelity universal gate set for ⁹Be⁺ ion qubits. Phys. Rev. Lett. 117, 060505 (2016).
- [23] Srinivas, R. et al. High-fidelity laser-free universal control of trapped ion qubits. Nature **597**, 209 (2021).
- [24] Clark, C. R. et al. High-fidelity Bell-state preparation with ⁴⁰Ca⁺ optical qubits. Phys. Rev. Lett. 127, 130505 (2021).
- [25] Weber, M. A. et al., Robust and fast microwave-driven quantum logic for trapped-ion qubits (2024).
- [26] Löschnauer, C. M. et al., Scalable, high-fidelity allelectronic control of trapped-ion qubits (2024).
- [27] Smith, M. C., Leu, A. D., Miyanishi, K., Gely, M. F. & Lucas, D. M. Single-qubit gates with errors at the 10⁻⁷ level. Phys. Rev. Lett. **134**, 230601 (2025).
- [28] Harty, T. P. et al. High-fidelity preparation, gates, memory, and readout of a trapped-ion quantum bit. Phys.

- Rev. Lett. 113, 220501 (2014).
- [29] An, F. A. *et al.* High fidelity state preparation and measurement of ion hyperfine qubits with $I > \frac{1}{2}$. Phys. Rev. Lett. **129**, 130501 (2022).
- [30] Sotirova, A. S. *et al.*, High-fidelity heralded quantum state preparation and measurement (2024).
- [31] Moehring, D. L. et al. Entanglement of single-atom quantum bits at a distance. Nature **449**, 68 (2007).
- [32] Stephenson, L. J. et al. High-rate, high-fidelity entanglement of qubits across an elementary quantum network. Phys. Rev. Lett. 124, 110501 (2020).
- [33] Krutyanskiy, V. et al. Entanglement of trapped-ion qubits separated by 230 meters. Physical Review Letters 130, 050803 (2023).
- [34] Saha, S. *et al.*, High-fidelity remote entanglement of trapped atoms mediated by time-bin photons (2024).
- [35] Drmota, P. et al. Robust quantum memory in a trappedion quantum network node. Phys. Rev. Lett. 130, 090803 (2023).
- [36] There is also a 5 % branching ratio for decays to the $D_{3/2}$ manifold, however these result in an unsuccessful entanglement attempt and so can be neglected.
- [37] Sackett, C. A. et al. Experimental entanglement of four particles. Nature 404, 256 (2000).
- [38] Genov, G. T., Schraft, D., Vitanov, N. V. & Halfmann, T. Arbitrarily accurate pulse sequences for robust dynamical decoupling. Phys. Rev. Lett. 118, 133202 (2017).
- [39] Letchumanan, V., Wilson, M. A., Gill, P. & Sinclair, A. G. Lifetime measurement of the metastable $4d^2D_{5/2}$ state in $^{88}\mathrm{Sr}^+$ using a single trapped ion. Phys. Rev. A **72**, 012509 (2005).
- [40] Nigmatullin, R., Ballance, C. J., De Beaudrap, N. & Benjamin, S. C. Minimally complex ion traps as modules for quantum communication and computing. New Journal of Physics 18, 103028 (2016).
- [41] Allcock, D. T. C. et al. omg blueprint for trapped ion quantum computing with metastable states. Applied Physics Letters 119, 214002 (2021).
- [42] Feng, L. et al. Realization of a crosstalk-avoided quantum network node using dual-type qubits of the same ion species. Nature Communications 15, 204 (2024).
- [43] Lai, P.-C. et al. Realization of a crosstalk-free two-ion node for long-distance quantum networking. Phys. Rev. Lett. 134, 070801 (2025).
- [44] Akerman, N. & Ozeri, R. Atomic combination clocks. New Journal of Physics 20, 123026 (2018).
- [45] Van Milligen, E. A., Gagatsos, C. N., Kaur, E., Towsley, D. & Guha, S. Utilizing probabilistic entanglement between sensors in quantum networks. Physical Review Applied 22, 064085 (2024).
- [46] Finkelstein, R. et al. Universal quantum operations and ancilla-based readout for tweezer clocks (2024). arXiv preprint arXiv:2402.16220.
- [47] Nguyen, N. H. et al. Demonstration of shor encoding on a trapped-ion quantum computer. Physical Review Applied 16, 024057 (2021).
- [48] Bourdeauducq, S. et al., m-labs/artiq: 6.0 (Version 6.0) (2021).
- [50] Revelle, M. C., Phoenix and Peregrine ion traps (2020).
- [51] Hayes, D., Khodjasteh, K., Viola, L. & Biercuk, M. J. Reducing sequencing complexity in dynamical quantum

- error suppression by Walsh modulation. Phys. Rev. A 84, 062323 (2011).
- [52] Hayes, D. et al. Coherent error suppression in multiqubit entangling gates. Phys. Rev. Lett. 109, 020503 (2012).
- [53] Wood, C. J., Biamonte, J. D. & Cory, D. G., Tensor networks and graphical calculus for open quantum systems (2015).
- [54] Řeháček, J., Hradil, Z., Knill, E. & Lvovsky, A. I. Diluted maximum-likelihood algorithm for quantum tomography. Phys. Rev. A 75, 042108 (2007).

SUPPLEMENTARY INFORMATION

S1. MODULES

Our quantum networking apparatus comprises two trapped-ion modules, Alice and Bob, which are connected via optical fibre links. Each module comprises a room-temperature micro-fabricated surface Paul trap fabricated by Sandia National Laboratories, housed in an ultra-high-vacuum chamber. In Alice, we use the HOA2 trap [49]; in Bob, we use the Phoenix trap [50] - the successor to the HOA2 trap. The traps feature two RF electrodes and 100 segmented DC control electrodes, enabling precise control over the trapping potentials and the execution of dynamic waveforms for ion shuttling, splitting and merging of ion crystals, and micromotion compensation. They also include a 60 μ m slot in the trap surface, providing optical access from the rear.

Each module has two imaging systems for collecting fluorescence from the ions. A rear-side imaging system collects $422\,\mathrm{nm}$ and $397\,\mathrm{nm}$ light through the slot in the trap chip, enabling simultaneous detection of both ion species. A front-side imaging system, comprising a $0.6\,\mathrm{NA}$ lens located outside the vacuum chamber, collects spontaneously-emitted $422\,\mathrm{nm}$ photons from the Sr^+ ion at its focal point and couples them into a single-mode optical fibre.

Each module is assigned a "host" computer, which is used to submit and schedule experiments, communicate with the experimental control system, and collect, analyse, and save experimental data. Real-time execution of experimental sequences are handled using the ARTIQ control system [48]. The majority of the hardware comprising this control system is from the Sinara ecosystem. A digital link connecting the control systems of the two modules provides a classical communication channel, enabling the exchange of information between the modules in real-time.

S2. LOCAL OPERATIONS

S2.1. Single-qubit gates

The ability to coherently manipulate individual qubits is a critical tool for universal quantum computing. We coherently manipulate the electronic state of the Sr⁺ ions using a narrow-linewidth 674 nm laser to address electric quadrupole transitions between sublevels of the S_{1/2} and D_{5/2} manifolds. In particular, we address the transition between $\left| \mathbf{S}_{1/2}, m_J = -\frac{1}{2} \right\rangle$ and $\left| \mathbf{D}_{5/2}, m_J = -\frac{3}{2} \right\rangle$, which forms the network qubit. We benchmark the single-qubit rotations of the network qubit using single-qubit randomised benchmarking (RBM). The results for both modules are given in Table S1.

We coherently manipulate states in the ground hyperfine manifold of the Ca⁺ ions using a pair of co-

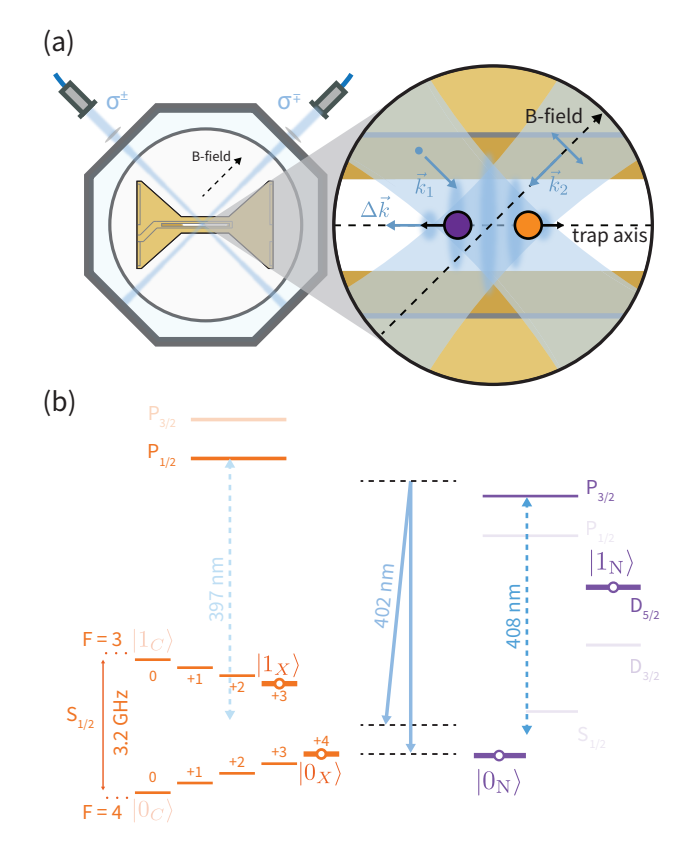


Fig. S1. Mixed-species entangling gates. (a) Geometry. Two orthogonal Raman beams at ~ 402 nm, with detuning $\Delta\omega$ with respect each other, drive a light-shift entangling gate between $^{43}\text{Ca}^+$ and $^{88}\text{Sr}^+$. See details in text. (b), Energy level diagram for $^{43}\text{Ca}^+$ and $^{88}\text{Sr}^+$ with the relevant levels used for the two-qubit gate.

propagating 402 nm Raman beams, detuned from each other by approximately 3.2 GHz. This choice of geometry allows us to minimise the relative wavevector of the two beams, and therefore the coupling to the ions' motion. We benchmark the performance of the single-qubit rotations of the circuit and auxiliary qubits using RBM; the results are given in Table S1.

S2.2. Two-qubit gates

The ability to perform logical entangling gates between ions of different species allows us to delegate roles for performing tasks which have diametric requirements, such as storing quantum information and realising a network interface. We perform these mixed-species entangling gates using light-shift mediated geometric phase gates [19].

As depicted in Fig. S1, the light-shift spin-dependent force is created using a single pair of intersecting 402 nm Raman beams, detuned from one another by $\Delta\omega$, which induce differential light-shifts of the ions' spin states.

Module	Qubit	State-prep. $(imes 10^{-3})$	Readout ($\times 10^{-3}$)			$egin{array}{c} 1Q ext{ gate} \\ ext{error} \\ ext{per Clifford} \\ ext{($ imes10^{-4}$)} \end{array}$	CNOT gate error per gate
			ϵ_0	ϵ_1	$\frac{\epsilon_0 + \epsilon_1}{2}$		
	\mathcal{Q}_{N}	4.7(5)	< 0.001	1.068(4)	0.534(2)	4.8(3)	
Alice	\mathcal{Q}_{C}	4.1(3)	4.1(4)	2.7(4)	3.4(4)	1.0(3)	0.024(2)
	\mathcal{Q}_{X}	3.1(4)	1.77(4)	0.357(4)	1.06(2)	1.4(3)	
	\mathcal{Q}_{N}	5.0(5)	< 0.001	1.085(4)	0.543(2)	9.8(3)	
Bob	\mathcal{Q}_{C}	4.6(3)	2.7(5)	1.7(5)	2.2(5)	1.2(4)	0.020(2)
	\mathcal{Q}_{X}	3.8(4)	1.02(2)	< 0.001	0.51(1)	1.2(3)	

Table S1. Summary of quantum operations within each module. Includes state preparation and measurement (SPAM) errors, single-qubit gate errors, and two-qubit CNOT gate errors.

At this wavelength, we couple most strongly to the $397\,\mathrm{nm}\ \mathrm{S}_{1/2}\leftrightarrow\mathrm{P}_{1/2}$ dipole transition in Ca^+ and the $408\,\mathrm{nm}\ \mathrm{S}_{1/2}\leftrightarrow\mathrm{P}_{3/2}$ dipole transition in Sr^+ , as shown in Fig. S1(a). The $\sim 10\,\mathrm{THz}$ detuning from these transitions suppresses unwanted single-photon scattering, while still providing a sufficiently strong driving force with moderate beam intensities. This configuration is advantageous since we can address both ion species with a single pair of beams.

The interference of the two beams results in a polarisation walking-standing wave propagating along the direction of the wavevector differential $\Delta \vec{k}$, as depicted in Fig. S1(b). The spin states of an ion held in this travelling-standing wave will experience a light-shift oscillating at $\Delta\omega$ with a phase depending on the position of the ion in the travelling-standing wave. The ions experience this spatially-dependent light-shift as a dipole force which drives motion along $\Delta \vec{k}$, with a sign and magnitude dependent on the spin state of the ion. By choosing the differential detuning of the Raman beams to be close to the secular frequency of one of the motional modes, i.e., $\Delta\omega = \omega_m + \delta$ where $|\delta| \ll \omega_m$, we off-resonantly drive the motional mode and coherently displace the spin states around approximately circular trajectories in the phase space of the motional mode.

The mass disparity between Sr⁺ and Ca⁺ results in large asymmetries in the radial mode participations of the ions, making these modes unsuitable for mediating entangling gates. Instead, we choose the axial out-of-phase (OOP) mode since each ion has a significant participation in the mode, and the "breathing" character of the ions' motion provides some suppression of the motional heating due to common-mode electric field noise. The Raman beams are therefore aligned in an orthogonal geometry such that their differential wavevector points in the axial direction and we can maximally drive the axial motion.

The coupling of the spin-dependent force to the spin

state depends on the ability to generate differential light shifts between the qubit states. However, for the Ca⁺ circuit qubits, the differential light shift is negligible, and thus the spin-dependent force will drive the states along the same phase-space trajectories, and so cannot be used to generate entanglement. We therefore drive the entangling gates using the auxiliary qubit instead. Furthermore, we apply the gate mechanism directly to the network qubit in Sr⁺—rather than the Zeeman ground state qubit, as done in Ref. [19]—which has the advantage of eliminating mapping pulses to convert between the Zeeman and optical qubit at the cost of reduced gate efficiency.

We employ 1st-order Walsh modulation [51, 52], a dynamical error suppression protocol which allows us to coherently suppress certain error processes occuring during the gate and symmetrises the phase space trajectories of the qubit states. This consists of dividing the gate interaction into two applications of the spin-dependent force, separated by $\hat{\sigma}_x$ rotations of each qubit. With the Walsh sequence, the asymmetries only result in a further reduction of the gate efficiency that is compensated for by the use of higher laser powers, but the same unitary can be achieved.

S2.2.1. CNOT gate

Through application of the Walsh-modulated spindependent force combined with single-qubit unitary operations, we implement a two-qubit CNOT gate between the network and auxiliary qubits. This mixed-species CNOT gate is a critical tool, enabling the local entanglement of the $\rm Sr^+$ and $\rm Ca^+$ ions for the creation of the GHZ states, and also the coherent transfer of quantum information between the two species of ions, discussed in Section S2.2.2.

We use Raman laser powers of approximately 20 mW

per beam, focussed to a beam waist of approximately 15 µm. With these parameters, we achieve mixed-species CNOT gates with a gate duration of $62 \,\mu s$ and $58 \,\mu s$ in Alice and Bob, respectively. We characterise the action of the CNOT gates using quantum process tomography. Quantum process tomography provides a complete characterisation of the gate process, enabling the reconstruction of the superoperators representing the actions of the two-qubit gates in each module. We reconstruct the superoperators for each module from $32\,400$ tomographic measurements. Compared to the ideal CNOT gate, we measure average gate fidelities of $97.6(2) \,\%$ and $98.0(2) \,\%$ for Alice and Bob, respectively.

S2.2.2. ISWAP gate

The ability to coherently transfer quantum information from Sr⁺ to Ca⁺ is an important resource in our trapped-ion modules, enabling the remote entanglement generated across the quantum network to be transferred from the Sr⁺ network qubit to the long-lived Ca⁺ circuit qubit.

The naive choice for implementing this transfer is the SWAP gate, which exchanges the quantum states of the participating qubits. The SWAP gate requires 3 instances of the CNOT gate and therefore significant errors can accumulate, particularly when the transfer is implemented in both modules. However, in typical scenarios, we only wish to map the state of the network qubit onto one of the Ca⁺ qubits, and thus the Ca⁺ ion will initially be in a known state, e.g., $|0_{\rm X}\rangle$. Hence, it is sufficient to implement the iSWAP gate, which requires only 2 instances of the CNOT gate.

The iSWAP circuit is shown in Fig. S2(a), and implements the unitary

$$\hat{U}_{\text{iSWAP}} = \begin{pmatrix} 1 & 0 & 0 & 0 \\ 0 & 0 & i & 0 \\ 0 & i & 0 & 0 \\ 0 & 0 & 0 & 1 \end{pmatrix}.$$

Thus, if we let the Sr^+ network qubit be in some arbitrary state $|\psi_N\rangle$ and the Ca^+ auxiliary qubit be prepared in the state $|0_X\rangle$, the iSWAP gate implements the mapping

$$|\psi_{N}\rangle|0_{X}\rangle \xrightarrow{\text{iSWAP}} |0_{N}\rangle \left(\hat{S}^{\dagger}|\psi_{X}\rangle\right) \in \mathcal{Q}_{N}\otimes\mathcal{Q}_{X}, \quad (S4)$$

where \hat{S} is the single-qubit Z rotation through $\pi/4$, given by the unitary matrix $\hat{S} = \text{diag}(1, i)$. We can then apply an \hat{S} -gate to the auxiliary qubit, completing the transfer of the state $|\psi_N\rangle$ from the Sr⁺ ion to the Ca⁺ ion.

As for the mixed-species CNOT-gate, we characterise the iSWAP gate using quantum process tomography to reconstruct superoperators, here from a total of $32\,400$ measurements. Compared to the ideal iSWAP-gate, we measure average gate fidelities of $95.9(2)\,\%$ and $96.0(2)\,\%$

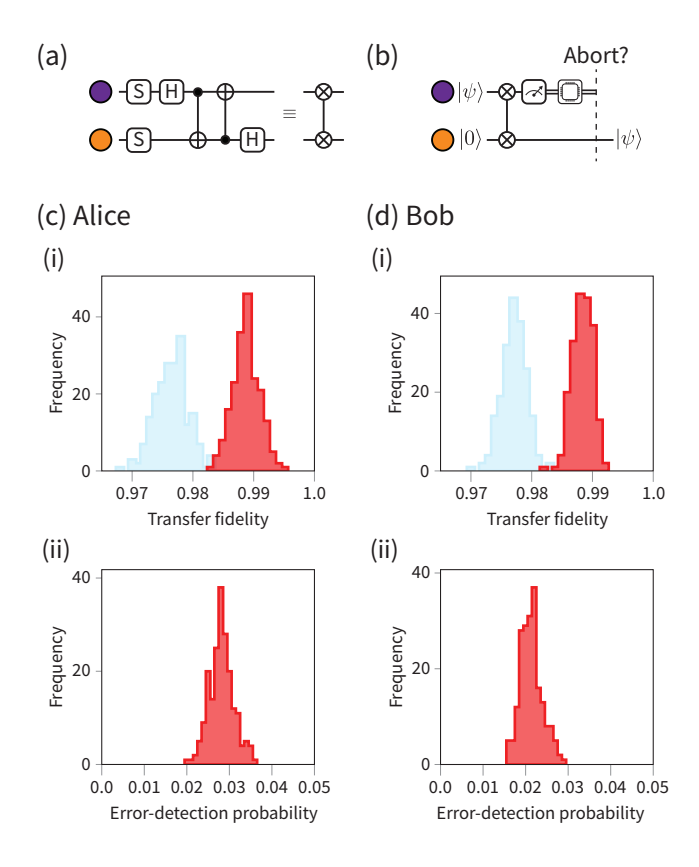


Fig. S2. iSWAP gate (a) iSWAP gate circuit. (b) iSWAP gate circuit with error-detection. (c)(i) and (d)(i) show the iSWAP transfer fidelities without error detection (light blue), and with error detection (red), for Alice and Bob, respectively. (c)(ii) and (d)(ii) show the error-detection probabilities, for Alice and Bob, respectively.

for Alice and Bob, respectively, consistent with that expected from the errors in the component gates.

Another important metric is the fidelity with which we transfer quantum information from the network qubit to the auxiliary qubit. From the reconstructed iSWAP superoperators, we can predict the action of the iSWAP-based state transfer, taking into account experimental imperfections. Such imperfections include imperfect state preparation of the auxiliary qubit and noise in the iSWAP gate.

Suppose imperfect state preparation of the auxiliary qubit yields the state

$$\hat{\tau}_0 = (1 - \epsilon) |0\rangle \langle 0| + \epsilon |1\rangle \langle 1| \in L(\mathcal{Q}_X), \quad (S5)$$

where ϵ is the state-preparation error and $L\left(\mathcal{Q}_{X}\right)$ denotes the space of density matrices for the auxiliary qubit. Additionally, let the noisy iSWAP process be represented by the superoperator $\hat{\mathcal{S}}_{\text{iSWAP}}$. The transfer process, described by

$$\mathcal{E}_{N\to X}: L(\mathcal{Q}_N) \to L(\mathcal{Q}_X),$$
 (S6)

is represented by the superoperator $\hat{\mathcal{S}}_{N\to X}$. This super-

operator is calculated as

$$\hat{\mathcal{S}}_{N \to X} = \hat{\mathcal{S}}_{S} \left(\hat{\mathbb{I}}_{Q_{X}}^{\otimes 2} \otimes \langle \langle \hat{\mathbb{I}}_{Q_{N}} | \right) \hat{\mathcal{V}}_{2} \hat{\mathcal{S}}_{iSWAP} \hat{\mathcal{V}}_{2}^{\dagger} \left(| \hat{\tau}_{0} \rangle \rangle \otimes \hat{\mathbb{I}}_{Q_{N}}^{\otimes 2} \right), \tag{S7}$$

where $\hat{\mathcal{V}}_2$ is the unravelling operation and $|\hat{A}\rangle$ denotes the vectorisation of the operator, \hat{A} , as in Ref. [53].

The ideal transfer process is effectively the identity operation

$$\mathcal{E}_{N\to X} (\hat{\rho} \in L(\mathcal{Q}_N)) = \hat{\rho} \in L(\mathcal{Q}_X),$$
 (S8)

and thus we can calculate the transfer fidelity as in [53],

$$\mathcal{F}_{N\to X} = \frac{d + \operatorname{tr}\left[\hat{\mathcal{S}}_{N\to X}\right]}{d(d+1)},$$
 (S9)

where $d = \dim(\mathcal{Q}_X) = \dim(\mathcal{Q}_N) = 2$. Histograms showing the spread of transfer fidelities, calculated from resampled iSWAP gate attempts, are shown for Alice and Bob in Fig. S2(c)(i) and (d)(i), respectively. We infer transfer fidelities of 97.8(3) % and 97.9(2) % for Alice and Bob, respectively.

Recalling Eq. S4, since the auxiliary qubit was (nominally) initially prepared in the computational state $|0_X\rangle$, the network qubit will (nominally) be left in the same state, $|0_N\rangle$. As a result of errors in the iSWAP gate or imperfect state preparation of the auxiliary qubit, the network qubit will occasionally be left in the "wrong" state. Therefore, following the iSWAP-gate, we perform a mid-circuit measurement of the network qubit: if we measure the network qubit in the state $|0_N\rangle$, we have projected the system into the $|0_N\rangle\langle 0_N|\otimes \hat{\mathbb{I}}_X$ subspace, and thus have effectively projected out part of the iSWAP gate error. If the measurement outcome yields the state $|1_N\rangle$, we simply restart the protocol. We perform this measurement and decision branching in real time.

The circuit for this error-detected iSWAP transfer is shown in Fig. S2(b). As before, we can use the reconstructed iSWAP superoperator to predict the action of the error-detected transfer in the presence of experimental imperfections, such as imperfect state preparation of the auxiliary qubit, noise in the iSWAP gate, and imperfect measurement of the network qubit.

As in the case of the non-error-detected transfer, we assume the imperfect state preparation of the auxiliary qubit is described by the state in Eq. S5 and that the noisy iSWAP gate is represented by the superoperator $\hat{\mathcal{S}}_{\text{iSWAP}}$. After the transfer, we make a measurement of the network qubit, and abort the experiment if we do not observe the qubit to be in the state $|0_N\rangle$. The positive operator-valued measure (POVM) corresponding to a measurement of the network qubit yielding the outcome $|0_N\rangle$ is given by

$$\hat{M}_0 = (1 - \epsilon_0) |0_{\mathcal{N}}\rangle \langle 0_{\mathcal{N}}| + \epsilon_1 |1_{\mathcal{N}}\rangle \langle 1_{\mathcal{N}}|.$$
 (S10)

We calculate the superoperator representing the error-

detected transfer process as

$$\hat{\mathcal{S}}'_{\mathrm{N}\to\mathrm{X}} = \hat{\mathcal{S}}_{S} \left(\hat{\mathbb{I}}_{\mathcal{Q}_{\mathrm{X}}}^{\otimes 2} \otimes \langle \langle \hat{M}_{0} | \right) \hat{\mathcal{V}}_{2} \hat{\mathcal{S}}_{\mathrm{iSWAP}} \hat{\mathcal{V}}_{2}^{\dagger} \left(| \hat{\tau}_{0} \rangle \rangle \otimes \hat{\mathbb{I}}_{\mathcal{Q}_{\mathrm{N}}}^{\otimes 2} \right). \tag{S11}$$

Note that since we have introduced an abort condition, the calculated process is no longer trace-preserving. Suppose the network qubit is prepared in some state $\hat{\rho}$ that we would like to transfer to the auxiliary qubit, then the probability that an error is detected, denoted p, can be calculated as

$$p = 1 - \operatorname{tr} \left[\mathcal{E}'_{N \to X} \left(\hat{\rho} \right) \right]. \tag{S12}$$

Note that, in general, this probability depends non-linearly on the input state, $\hat{\rho}$, and thus it is not possible to normalise the process.

We calculate the average gate fidelity for the errordetected transfer using a Monte-Carlo approach. We sample N input states $|\psi_i\rangle$ from the Haar measure and compute the average transfer fidelity as

$$\bar{\mathcal{F}}_{N \to X} = \frac{1}{N} \sum_{i=1}^{N} \frac{\langle \psi_i | \mathcal{E}'_{N \to X} (|\psi_i\rangle \langle \psi_i|) |\psi_i\rangle}{\operatorname{tr} \left[\mathcal{E}'_{N \to X} (|\psi_i\rangle \langle \psi_i|)\right]}.$$
 (S13)

We calculate the average error-detection probability, \bar{p} , in similar fashion, as

$$\bar{p} = 1 - \frac{1}{N} \sum_{i=1}^{N} \operatorname{tr} \left[\mathcal{E}'_{N \to X} \left(|\psi_i\rangle \left\langle \psi_i | \right) \right]. \tag{S14}$$

Histograms showing the spread of average transfer fidelities, $\bar{\mathcal{F}}_{N\to X}$, and error-detection probabilities, \bar{p} , as calculated from iSWAP gates reconstructed from resampled datasets, are shown in Fig. S2(c) and (d) for Alice and Bob, respectively. The results for Alice (Bob) indicate an average transfer fidelity of $\bar{\mathcal{F}}_{N\to X} = 99.0(2)\%$ ($\bar{\mathcal{F}}_{N\to X} = 99.0(2)\%$) and an average error-detection probability of $\bar{p} = 2.8(3)\%$ ($\bar{p} = 2.2(3)\%$).

S2.3. Hyperfine transfer

Since the circuit qubit does not participate in the mixed-species gate, the gate interaction is performed between the network and auxiliary qubits. Consequently, we require the ability to coherently inter-convert between the circuit and auxiliary qubit before and after the local operations. This mapping is performed using the Raman beams to coherently address the transitions within the ground hyperfine manifold of 43 Ca⁺.

As in Ref. [4], the transfer of the circuit qubit to the auxiliary qubit begins with the mapping of the state $|0_{\rm C}\rangle$ to the state $|0_{\rm X}\rangle$. However, due to the near degeneracy of the transition $\mathcal{T}_0:|0_{\rm C}\rangle\leftrightarrow|F=3,M_F=+1\rangle$ and the transition $\mathcal{T}_1:|1_{\rm C}\rangle\leftrightarrow|F=4,M_F=+1\rangle$, separated by only $\Delta f\approx 15\,{\rm kHz}$, it is not possible to map the $|0_{\rm C}\rangle$ state out of the circuit qubit without off-resonantly driving population out of the $|1_{\rm C}\rangle$ state. We suppress this

off-resonant excitation using a composite pulse sequence comprising three pulses resonant with the \mathcal{T}_0 transition, with pulse durations equal to the 2π -time of the \mathcal{T}_1 transition, and phases optimised to minimise the off-resonant excitation. This pulse sequence allows us to simultaneously perform a π -pulse on the \mathcal{T}_0 transition and an identity on the off-resonantly-driven \mathcal{T}_1 transition. Raman π -pulses are then used to complete the mapping to the $|0_X\rangle$ state. Another sequence of Raman π -pulses coherently maps $|1_C\rangle \to |1_X\rangle$, thereby completing the transfer of the circuit qubit to the auxiliary qubit, $\mathcal{Q}_C \to \mathcal{Q}_X$. To implement the mapping $\mathcal{Q}_X \to \mathcal{Q}_C$ the same pulse sequence is applied in reverse.

We characterise our $\mathcal{Q}_C \leftrightarrow \mathcal{Q}_X$ transfer sequence by performing a modification of single-qubit RBM, in which we alternate Clifford operations on the \mathcal{Q}_C and \mathcal{Q}_X qubits. We measure an error per transfer of $3.8(2) \times 10^{-3}$ $(2.6(1) \times 10^{-3})$ for Alice (Bob).

S3. QUANTUM STATE TOMOGRAPHY

To characterise the states generated in the experiments described in the main text, we use two methods: full state tomography and partial state tomography.

S3.1. Full state tomography

A density matrix, $\hat{\rho} \in L(\mathcal{Q})$, provides a complete description of the quantum state of a system. Quantum state tomography is the process by which measurements of a number of copies of a state are used to reconstruct the density matrix describing the state of a system.

Suppose we have N of copies of some unknown quantum state that we can measure using some measurement apparatus. Our measurement apparatus has a number of different measurement settings, labelled by the index i, and each measurement setting has a set of possible outcomes, labelled by the index j. The measurement outcomes for a particular measurement setting are associated with the POVMs, \hat{M}_{ij} , satisfying $\sum_j \hat{M}_{ij} = \hat{\mathbb{I}}$, such that the probability that a measurement of the state using the measurement setting i yields the outcome j is given by

$$p_{ij} = \operatorname{tr}\left[\hat{M}_{ij}\hat{\rho}\right].$$
 (S15)

Suppose we make measurements of N copies of our state using different measurement settings and count the number of occurrences, n_{ij} , of each outcome for each measurement setting. The likelihood of obtaining a particular dataset, $\{n_{ij}\}$, given the state $\hat{\rho}$, can be written as

$$\mathcal{L}\left(\hat{\rho}\right) = \Pi_{ij} \left(\operatorname{tr} \left[\hat{M}_{ij} \hat{\rho} \right] \right)^{n_{ij}}. \tag{S16}$$

Therefore, we can find an estimate for the density matrix describing the state of the system by finding the density matrix, $\hat{\rho}$, which maximises the likelihood in Eq. S15.

After performing the tomographic measurements and collecting the raw data, we find the density matrix that maximises the likelihood by following an iterative diluted maximum-likelihood estimation algorithm developed in Ref. [54].

For a system comprising N qubits, the tomographic measurements are constructed by randomly selecting a measurement setting, i, for each qubit. We perform a measurement with this setting by applying a single-qubit rotation

$$\hat{U}_{i} \in \left\{ \hat{\mathbb{I}}, \ \hat{\mathbb{I}}, \ \hat{R}_{X}\left(\frac{\pi}{2}\right), \ \hat{R}_{Y}\left(\frac{\pi}{2}\right), \ \hat{R}_{X}\left(-\frac{\pi}{2}\right), \ \hat{R}_{Y}\left(-\frac{\pi}{2}\right) \right\},$$
(S17)

to the $n^{\rm th}$ qubit and measuring in the computational basis, $\hat{\sigma}_z$. This corresponds to a measurement of the observable $\hat{U}_i^{\dagger}\hat{\sigma}_z\hat{U}_i$. Note that the set of rotations in Eq. S17 corresponds to a tomographically over-complete set of measurements, as we measure along the $\pm X$ and $\pm Y$ directions, which improves robustness to systematic errors. Note that when selecting a measurement setting, we include the $\hat{\mathbb{I}}$ element twice, ensuring that we acquire equal statistics along each axis.

Assuming perfect single-qubit rotations and qubit readout, the POVMs for the $m^{\rm th}$ qubit can be written as

$$\hat{M}_{i_m,0} = \hat{U}_i^{\dagger} |0\rangle \langle 0| \hat{U}_i, \tag{S18}$$

$$\hat{M}_{i_m,1} = \hat{U}_i^{\dagger} |1\rangle \langle 1| \hat{U}_i. \tag{S19}$$

Thus, the N-qubit POVMs may be constructed as

$$\hat{M}_{ij} = \bigotimes_{m=1}^{N} \hat{M}_{i_m, j_m}, \tag{S20}$$

where the overall measurement setting, i, is the collection of single-qubit measurement settings, (i_1, i_2, \ldots, i_N) , and the overall measurement outcome, j, is the collection of the individual single-qubit measurement outcomes, (j_1, j_2, \ldots, j_N) .

Thus far, we have assumed perfect tomographic measurements. Now, to obtain a more accurate characterisation of the quantum system, we incorporate imperfect qubit readout into our algorithm. Let ϵ_0 and ϵ_1 denote the readout errors of qubit states, such that ϵ_0 (ϵ_1) corresponds to the probability that a measurement of a qubit prepared in the state $|0\rangle$ ($|1\rangle$) will yield the measurement outcome 1 (0). We therefore construct the single-qubit tomographic measurement POVMs as

$$\hat{M}_{i,0} = (1 - \epsilon_0) \hat{U}_i^{\dagger} |0\rangle \langle 0| \hat{U}_i + \epsilon_1 \hat{U}_i^{\dagger} |1\rangle \langle 1| \hat{U}_i, \quad (S21)$$

$$\hat{M}_{i,1} = (1 - \epsilon_1) \hat{U}_i^{\dagger} |1\rangle \langle 1| \hat{U}_i + \epsilon_0 \hat{U}_i^{\dagger} |0\rangle \langle 0| \hat{U}_i.$$
 (S22)

Experimentally determined values for the readout errors, ϵ_0 and ϵ_1 , for the different qubits are given in Table S1. We neglect errors in the single-qubit rotations as we do not yet have a complete understanding of the structure of these errors, however, we expect this to be $< 1 \times 10^{-3}$.

Once we have reconstructed a state $\hat{\rho}$, we can calculate the *fidelity* of the state to some target pure state, $|\psi\rangle$, as

$$\mathcal{F}(\hat{\rho}, |\psi\rangle \langle \psi|) = \langle \psi | \hat{\rho} | \psi \rangle. \tag{S23}$$

For the characterisation of bipartite states, we make use of the *entanglement fidelity*, \mathcal{F}_E , which is defined as the fidelity to the closest maximally entangled state under local operations,

$$\mathcal{F}_E = \max_{\hat{U}} \mathcal{F} \left(\hat{U} \hat{\rho} \hat{U}^{\dagger}, \left| \Phi^+ \right\rangle \right), \tag{S24}$$

where $\hat{U} = \hat{U}_1 \otimes \hat{U}_2$ and $|\Phi^+\rangle$ is a Bell state. For the GHZ states, we define the entanglement fidelity as the fidelity of the state to the GHZ state under local Z rotations, such that for N qubits

$$\mathcal{F}_E = \max_{\hat{U}} \mathcal{F} \left(\hat{U} \hat{\rho} \hat{U}^{\dagger}, |\text{GHZ}_N\rangle \right),$$
 (S25)

where $\hat{U} = \bigotimes_{i=1}^{N} \hat{R}_{Z}(\phi_{i})$ and $|GHZ_{N}\rangle$ is the N-qubit GHZ state.

S3.2. Partial state tomography

Full quantum state tomography provides a complete characterisation of an unknown quantum state; however, it is expensive in the number of measurements required to achieve a particular precision. However, given prior knowledge about what form the state should take, partial state tomography via population and parity measurements can be an inexpensive way to extract information about particular properties of the state.

Let us write the states that we create as the density matrix

$$\hat{\rho} = \sum_{i,j} \rho_{i,j} |i\rangle \langle j| \in L\left(\mathcal{Q}^{\otimes N}\right), \tag{S26}$$

where $|i\rangle \in \mathcal{Q}^{\otimes N}$. The fidelity of the created state to the desired state, Eq. 1, is given by

$$\begin{split} \mathcal{F} &= \langle \psi | \, \hat{\rho} \, | \psi \rangle \\ &= \frac{1}{2} \left[\rho_{0...0,0...0} + \rho_{1...1,1...1} + 2 | \rho_{0...0,1...1} | \cos \left(\varphi \right) \right], \end{split}$$

where $\varphi = \arg(\rho_{0...0,1...1})$. Let us now define the population observable, $\hat{P} = \hat{\Pi}_0^{\otimes N} + \hat{\Pi}_1^{\otimes N}$, such that

$$P = \left\langle \hat{P} \right\rangle = \rho_{0...0,0...0} + \rho_{1...1,1...1}. \tag{S27}$$

Furthermore, define the parity observable, $\hat{\sigma}_{\phi}^{\otimes N}$, where $\hat{\sigma}_{\phi} = \cos(\phi) \hat{\sigma}_x + \sin(\phi) \hat{\sigma}_y$, such that for states of the form Eq. 1, we have

$$\left\langle \hat{\sigma}_{\phi}^{\otimes N} \right\rangle = C \cos\left(N\phi - \varphi\right),$$
 (S28)

where $C=2|\rho_{0...0,1...1}|$ and φ is the parity phase of the created state. Thus, if we define the fidelity of the created state to the state in Eq. 1 up to an arbitrary Z-rotation, we find that the fidelity is given by

$$\mathcal{F} = \frac{P+C}{2}.\tag{S29}$$

Experimentally, the population measurement can be performed by simply measuring the created state in the computational basis, and computing the expectation value $\langle \hat{P} \rangle$, i.e., the probability that the qubits were all measured to be in the same state, e.g., $P_{00} + P_{11}$ for the 2-qubit case. The parity measurements can be implemented by first performing $\hat{R}_{\phi+\pi/2}$ ($\pi/2$) rotations on each qubit, before measuring in the computational basis. This corresponds to a measurement of the qubits along the axis at an angle ϕ to the X-axis in the XY-plane of the Bloch sphere, associated with the operator $\hat{\sigma}_{\phi}$. We thus use these measurement outcomes to calculate the expectation values, $\langle \hat{\sigma}_{\phi}^{\otimes N} \rangle$.

S4. TOMOGRAPHICALLY RECONSTRUCTED DENSITY MATRICES

In Figs. S3-S7, we provide the reconstructed density matrices for the states generated by the experiments described in the manuscript. These density matrices yield the entanglement fidelities quoted in the manuscript.

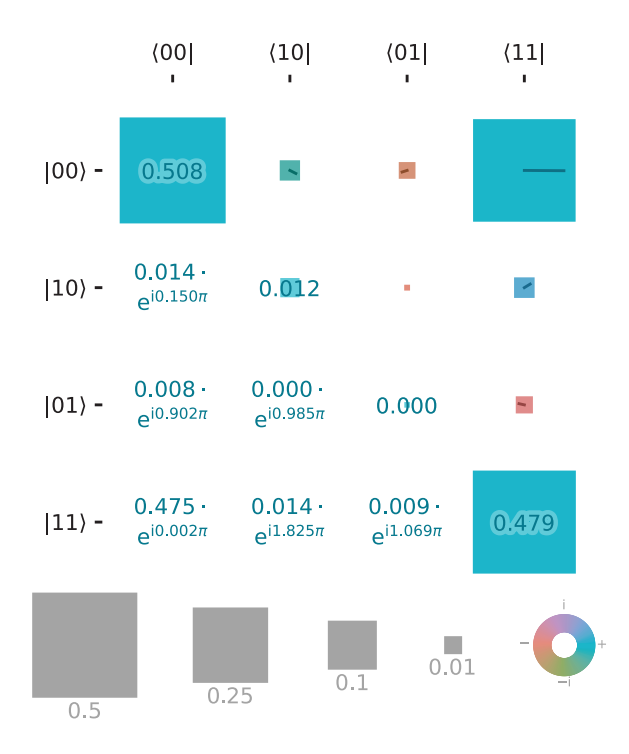


Fig. S3. Tomographic reconstruction of Sr^+ - Sr^+ remotely entangled state. The reconstructed density matrix yields an entanglement fidelity of 96.94(9)%.

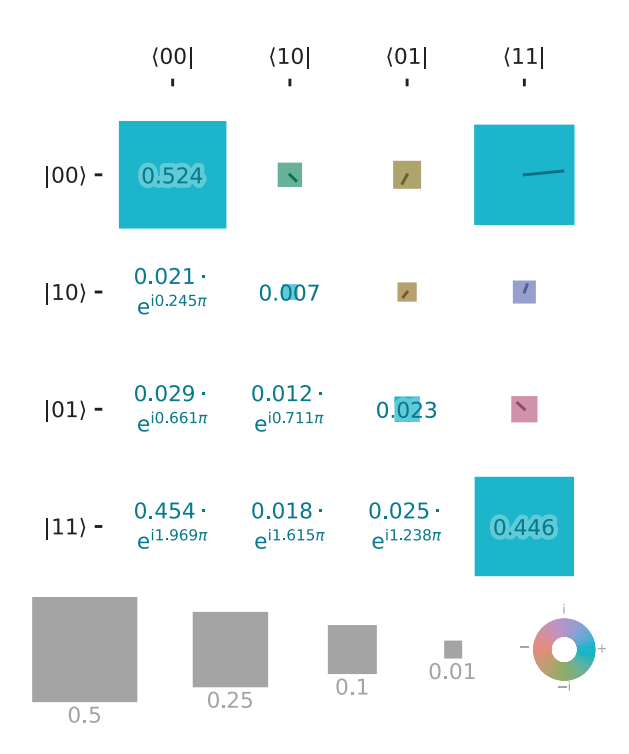


Fig. S4. Tomographic reconstruction of Sr⁺-Ca⁺ remotely entangled state. The reconstructed density matrix yields an entanglement fidelity of 94.1(6) %.

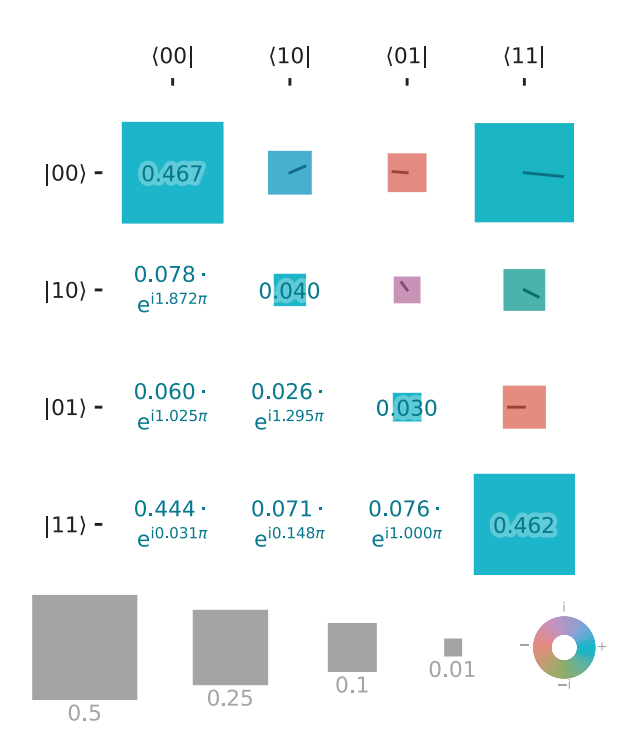


Fig. S5. Tomographic reconstruction of Ca⁺-Ca⁺ remotely entangled state. The reconstructed density matrix yields an entanglement fidelity of 93.1(7) %.

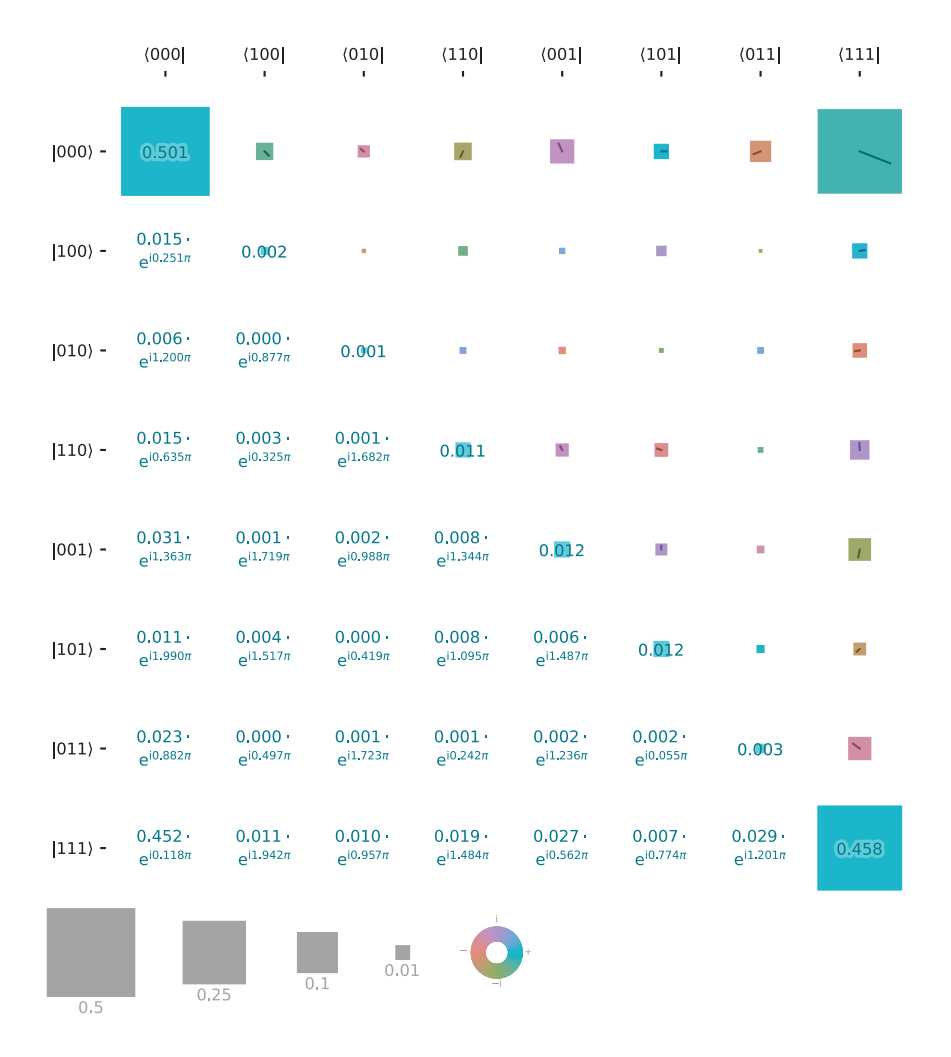


Fig. S6. Tomographic reconstruction of $Sr^+-Sr^+-Ca^+$ remotely entangled state. The reconstructed density matrix yields an entanglement fidelity of 93.1(7)%.



Fig. S7. Tomographic reconstruction of Sr⁺-Sr⁺-Ca⁺-Ca⁺ remotely entangled state. The reconstructed density matrix yields an entanglement fidelity of 91.9(8) %.